processes

MDPI

Article

Research on the Heat Extraction Performance Optimization of Spiral Fin Coaxial Borehole Heat Exchanger Based on GA–BPNN–QLMPA

Biwei Fu [1,2], Zhiyuan Guo [1,2], Jia Yan [3,*], Lin Sun [1,2], Si Zhang [1,2] and Ling Nie [2]

1 Cooperative Innovation Center of Unconventional Oil and Gas, Yangtze University (Ministry of Education & Hubei Province), Wuhan 430100, China; fubiwei@yangtzeu.edu.cn (B.F.); guozhiyuanzy@163.com (Z.G.); 202072577@yangtzeu.edu.cn (L.S.); zhangsi@yangtzeu.edu.cn (S.Z.)
2 School of Mechanical Engineering, Yangtze University, Jinzhou 434023, China; 200520@yangtzeu.edu.cn
3 Institute of Exploration Techniques, CAGS, Langfang 065000, China
* Correspondence: yj18531665717@163.com

Abstract: Geothermal energy, a renewable energy source with enormous reserves independent of the external environment, is essential for reducing carbon emissions. Spiral fin coaxial borehole heat exchanger (SFCBHE) is vital for geothermal energy extraction. Its heat extraction performance requires further improvements for efficient performance that consider the structural sizes and installation positions of the SFCBHE and the nonlinear coupling with respect to several factors. The heat extraction performance of SFCBHE is optimized using a combination of genetic algorithm–back-propagation neural network (GA–BPNN) and the Q-learning-based marine predator algorithm (QLMPA). This study analyzes and compares the effects of geothermal energy extraction of smooth pipe TY-1, structure before optimization TY-2, and optimized structure TY-3. Following optimization with GA–BPNN–QLMPA, the heat extraction performance of TY-3 is enhanced by 30.8% and 23.6%, respectively. The temperature of maximum extraction is improved by 26.8 K and 24.0 K, respectively. The power of maximum heat extraction is increased by 148.2% and 109.5%, respectively. The optimization method can quickly and accurately determine the heat extraction performance for different structural sizes and installation positions of the SFCBHE. These findings are crucial for developing high-performance SFCBHE and efficiently using geothermal energy.

Keywords: geothermal exploitation; coaxial borehole heat exchanger; performance evaluation factor; Q-learning-based marine predator algorithm; heating power

Citation: Fu, B.; Guo, Z.; Yan, J.; Sun, L.; Zhang, S.; Nie, L. Research on the Heat Extraction Performance Optimization of Spiral Fin Coaxial Borehole Heat Exchanger Based on GA–BPNN–QLMPA. *Processes* **2023**, *11*, 2989. https://doi.org/10.3390/pr11102989

Academic Editor: Iztok Golobič

Received: 16 September 2023
Revised: 11 October 2023
Accepted: 14 October 2023
Published: 17 October 2023

1. Introduction

As a clean, low-carbon, safe, and stable renewable energy, geothermal energy is the only indigenous renewable energy unaffected by weather and seasonal changes. It can be used for heating, power generation, cooling, agricultural cultivation, and other fields. It is gradually emerging as one of the most important means for countries to promote the "Carbon Peak" and "Carbon neutrality" objectives [1–3]. Hydrothermal geothermal energy is the primary geothermal energy that is currently exploited and utilized. It generally refers to the geothermal energy buried in hot water at the depth range of 200~3000 m, primarily in the form of liquid moisture or steam, etc. [4,5]. The coaxial drilled heat exchanger (CBHE) has become the principal hydrothermal geothermal energy extraction method as a result of its low costs, low development issues, and high heat extraction performance [6,7]. Its heat extraction performance is a crucial factor affecting the effectiveness of geothermal energy extraction. CBHE consists of the inner and outer casing, and the outer casing is manufactured from steel pipe, which is fixed in the surrounding geotechnical stratum with high thermal conductivity cement (its thermal conductivity can reach 3.0 W/m·K or higher) to achieve efficient geothermal energy absorption. The inner casing is fastened in the outer casing. Low thermal conductivity materials, such as polyethene and polypropylene, are used for heat insulation and adiabatic treatment to prevent the heat of the extracted water from being transferred backward to the annular air channel and reduce thermal power loss [8–12].

To increase the effects of geothermal energy extraction, how to strengthen the heat extraction performance of CBHEs has been widely discussed by experts. The research primarily focuses on two aspects: (1) changing the structure and material and (2) transforming the medium or method. Among them, changing the structure and material has significantly affected heat extraction performance, which has been the research focus in recent years. For example, Zanchini et al. examined the effects of CBHE cross-section composition materials and geometric configurations. They significantly reduced the impact of thermal short-circuiting by adopting low thermal conductivity materials for the inner tube. The performance of CBHE can be increased by increasing the diameter of the inner tube while keeping the outer tube unchanged [13]. Chen et al. established three-dimensional geometrical models of double-U BHE and intermittently arranged helical ring fin–enhanced CBHE and used an equivalent cross-section area of the embedded tube to upgrade and replace the double-U BHE model. The results demonstrate that the linear heat transfer of the enhanced coaxial BHE is significantly better than that of the equivalent U-type BHE [14]. Gascuel et al. analyzed the effect of depth, inner tube material, and well diameter on heat transfer performance using numerical simulations. They concluded that optimal performance was obtained from the deepest and largest diameter wells by selecting HDPE for the inner tube material [15]. Linrui Jia et al. developed an improved varied heat flux model for the CBHE using the superposition method, taking the vertical inhomogeneity of the specific heat flux into account. The improved analytical model can provide an accurate and efficient method for this inhomogeneous problem and a valuable tool for designing and optimizing CBHEs for actual engineering applications [16]. Mostafa M. Abdelhafiz et al. presented an application of a thermal transient model to a coaxial borehole heat exchanger system. The results showed that the reverse circulation had a better heat extraction, while regular flow performed better in the case of heat injection [17]. Taha Rajeh et al. introduced a detailed comparative numerical study on a novel CGHE with an oval cross-section for enhancing the performance of the GCHP. The results revealed that oval-CGHE significantly surpasses the conventional circle-CGHE, improving the maximum and average heat transfer greatly [18]. Sun et al. compared and analyzed the heat transfer performance of three types of CBHE with vortex generator with that of the conventional structure and concluded that the spiral fin coaxial borehole heat exchanger (SFCBHE) has the best performance [19]. Previous studies examining the effect of a single influencing factor on the efficiency of geothermal energy extraction have yielded many meaningful conclusions. The actual extraction process of geothermal energy is affected by several nonlinear coupling factors, such as heat exchanger structural parameters and process parameters. Therefore, considering the structural size and installation position of SFCBHE and other nonlinear coupling factors, the study of the heat extraction performance of SFCBHE can better fulfill the requirements of complex working conditions.

Machine learning offers a decisive advantage in multifactor nonlinear coupling agent models. Pérez-Zárate et al. used an artificial neural network (ANN) approach to predict the deep reservoir temperature [20]. Tut Haklidir and Haklidir developed a deep learning model to predict geothermal reservoir temperatures. Their results demonstrated that the deep neural network (DNN) algorithm exhibits lower errors than linear regression and support vector machine regression (SVR) [21]. Jery et al. simulated a geothermal heat exchanger, investigated the optimal diameter and nanoparticle concentration, and presented the use of ANN models to predict the Nusselt number and entropy based on numerical results. These models could achieve the mean absolute error (MAE) below 3% and R^2 (goodness of fit) above 0.95 [22]. The above scholars used ANNs and DNNs to predict geothermal reservoir temperatures, geothermal water temperatures in different regions, and Nusselt numbers, thus achieving better results. However, ANNs and DNNs are elementary to fall into the local minima, causing significant errors in the results. In sequence, to obtain a model with higher accuracy, other algorithms can be implemented to optimize the initial weights and thresholds to avoid the problem of falling into a local minimum. A genetic algorithm (GA) can automatically acquire and accumulate knowledge of the search space during the search process and adaptively control the search process to obtain the optimal solution [23]. Therefore, the GA optimizing back-propagation neural network (GA–BPNN) can be applied to construct the agent model for the case of multifactorial nonlinear coupling of structural size and installation position of SFCBHE. The agent model obtained by GA–BPNN is taken as the fitness function to determine the optimal parameter combinations. Furthermore, an optimization algorithm must be used to determine the global optimum value of the agent model and the corresponding parameter combinations. Since the Marine Predator algorithm (MPA) has significant advantages in engineering optimization problems [24,25], which, combined with the Q-learning algorithm, accelerates the convergence of the standard MPA [26], QLMPA can be applied to optimize the heat extraction performance of the SFCBHE.

In our previous research work [19,27], the heat transfer performance of coaxial drilled heat exchangers with three different shapes vortex generators was compared with that of traditional heat exchangers without vortex generators, and it was concluded that the helical fin coaxial drilled heat exchangers had the best performance. To improve the heat extraction performance of SFCBHE, based on previous research, a numerical simulation model is constructed to optimize the heat extraction performance under the coupling of structural size and installation position of SFCBHE using GA–BPNN–QLMPA with PEC as the evaluation indicator. This optimization method can predict the heat transfer performance of different structural sizes and installation positions of the heat exchanger and calculate the optimal parameter combinations of the high-performance SFCBHE, providing a theoretical foundation for the development of the high-performance SFCBHE and is crucial for the advancement of highly efficient geothermal energy mining technology.

2. Numerical Model and Validation

2.1. Geometric Model

SFCBHE is primarily applied to 200~3000-m-deep hydrothermal geothermal energy resource extraction, which comprises cement, casing, heat pump, circulating pump, inner tube, and vortex generator. The bottom of the well is blocked with cement to create a closed circulating channel.

Principle of SFCBHE: The circulating pump injects the fluid at a lower temperature into the hollow part. The fluid absorbs the heat from the formation rock and warms the injected supercooled liquid. After passing through the spiral fins, the fluid strengthens the mixing characteristics of the fluid flow. It destroys the boundary layer on the near-wall surface to maintain the heat transfer [19].

After reaching the bottom of the well, due to the stratum and ground circulation pump pressure, the bottom of the hot fluid flows to the inner tube. Under the action of the heat pump for the city heating, the fluid after heating and then through the circulating pump into the next cycle to achieve the effect of "taking heat but not water". The principle of the system is depicted in Figure 1a. As the ground temperature gradient effect, the bottom of the well has the highest heat. For a better study of the heat transfer performance, the best heat transfer performance was determined from the bottom of the 10-m-deep borehole for the survey. Figure 1b presents its structural size. The geometric size is shown in Table 1. The distance of the vortex generator (DOTVG) is an abbreviation for the distance of the vortex generator from the bottom of the inner tube. The fin height is an abbreviation for the size of the helical fins, the pitch is an abbreviation for the pitch of the vortex generator, and the depth of insertion of the inner tube (TDIT) is an abbreviation for the distance of the lower end of the insulated tube from the bottom of the well. TL is an abbreviation for the total length of SFCBHE. OTD is an abbreviation for the outer tube diameter. ITI is an abbreviation for the insulation tube inner diameter. TVGD is an abbreviation for the vortex generator's diameter.

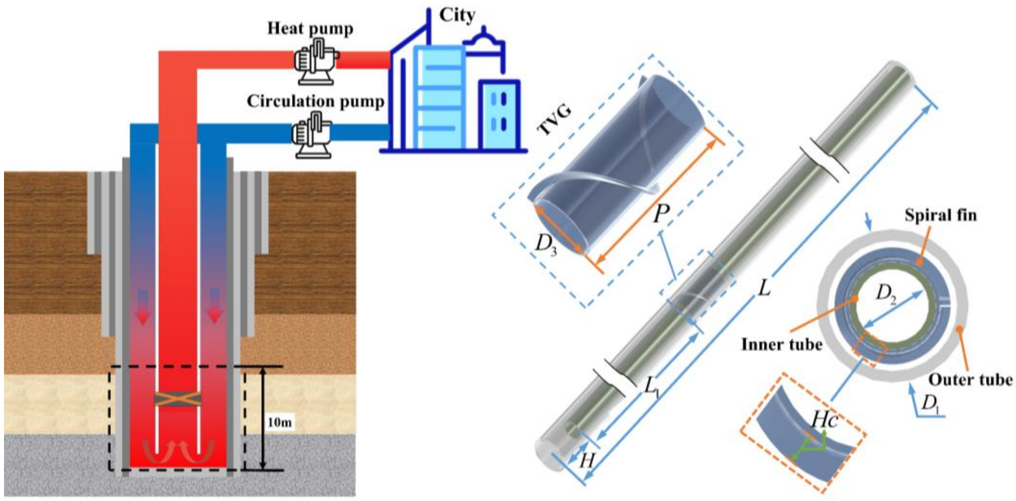

(**a**) SFCBHE system principle (**b**) SFCBHE 3D model

Figure 1. SFCBHE system and the bottom of 10 m.

Table 1. Fixed and optimized parameters for 10-m-deep SFCBHE.

Type	Parameter	Symbol	Initial Value	Ranges
Fixed parameters	DOTVG	L_1	2850 mm	—
	TL	L	10,000 mm	—
	OTD	D_1	210 mm	—
	ITI	D_2	100 mm	—
	TVGD	D_3	130 mm	—
Optimized parameters	fin height	HC	15 mm	5~20 mm
	pitch	P	300 mm	100~400 mm
	Number of fins	F	1	1~4
	Number of TVG	G	1	1~4
	TDIT	H	200 mm	100~700 mm

2.2. Numerical Model and Evaluation Indicator

2.2.1. Model Assumption

The simulation of the numerical value is challenging for considering the complex heat transfer process of the heat exchanger under actual working conditions. For this reason, the following reasonable assumptions are made [19]:

(1) The geotechnical soil around the geothermal well is assumed to be a homogeneous medium, groundwater seepage is neglected, and the heat transfer in the underground geotechnical soil is considered pure heat conduction.
(2) The heat source at the well's bottom and the surface temperature are considered constant.
(3) The geotechnical soil's surface temperature and thermophysical parameters change only along the depth direction.
(4) It is assumed that the buried pipe, the backfill material, and the ground are closed in contact and that there is no contact thermal resistance between them.

2.2.2. Control Equations and Boundary Conditions

(1) Control Models

Sun et al. [19] demonstrated that strong cyclonic flow forms after the fluid passes through the SFCBHE, using the (RNG) k–ε turbulence model, which is better for eddies and strong curvature. Similarly, the Navier–Stokes (RANS) model is better for the control equations [28].

(2) Boundary conditions and meshing

Heat conduction pipe and insulation pipe are placed between the annular region for the inlet. The inlet boundary is defined as the velocity inlet. The middle insulation pipe is the medium outlet after heat transfer, and the outlet boundary is identified as the pressure outlet.

The heat transfer boundary condition between the circulating fluid in the tube and the tube wall surface is defined as the coupled heat transfer boundary. In the analysis, the surface temperature is taken as 300 K, the depth of the well is 2667 m, the temperature gradient of the excellent wall is T_g = 4.5 K/100 m [29,30], and the temperature at the bottom boundary of SFCBHE is 420 K according to Equation (1). The temperature boundary is applied to the excellent wall by using the UDF control in the model. Figure 2a depicts the specific boundary setting.

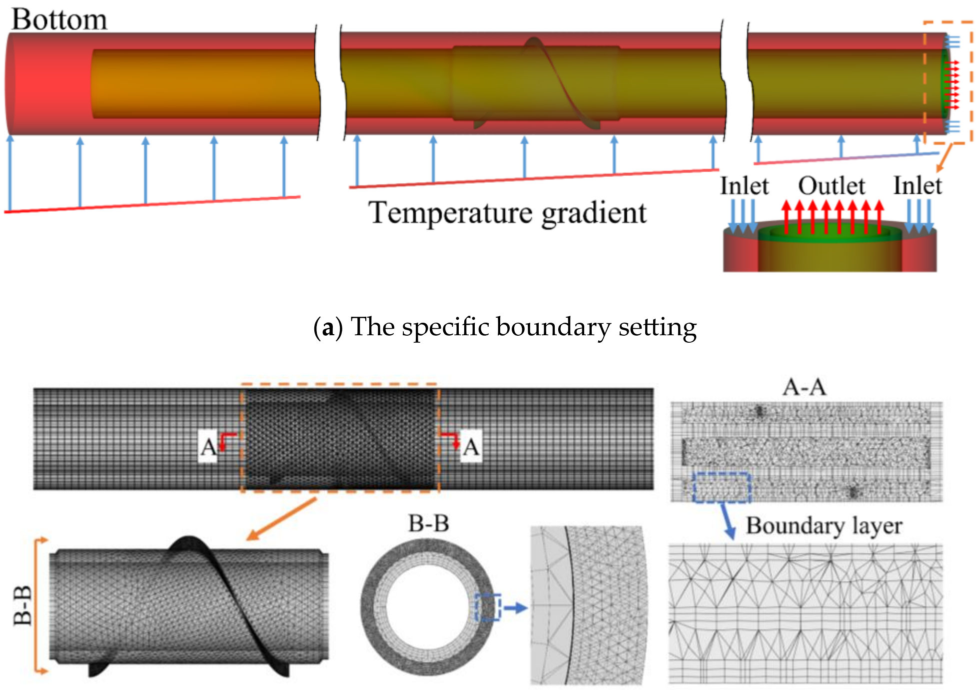

(**a**) The specific boundary setting

(**b**) The meshing scheme of the SFCBHE

Figure 2. SFCBHE Boundary conditions and meshing.

(1) Rock temperature

$$T_W = T_{sur} + T_g z \tag{1}$$

where T_W is the rock temperature, K; T_{sur} is the ground surface temperature, K; T_g is the land temperature gradient, K/m; z is the well depth, m.

(2) Outlet pressure

$$P_{out} = \rho g z \tag{2}$$

Figure 2b shows the meshing scheme of the SFCBHE, with a hexahedral structured mesh for the insulated tube and an unstructured tetrahedral mesh for the spiral fin part. The impact of the near-wall boundary layer on heat transfer is considered. Boundary layer encryption and mesh refinement are conducted at the interface between the tube wall and the fluid and on the spiral fin surface to better capture the turbulence characteristics and deal with the viscous sublayer effect near the tube wall. The grid independence verification has been performed. When the inlet velocity V_{in} = 0.1 m/s, the variation of Nussel number *Nu* and friction coefficient *f* of SFCBHE with the number of grids are shown in Figure 3. As shown in Figure 3, when the number of grids exceeds 620 thousands, *Nu* and *f* basically remain unchanged with the increase of grids number. Therefore, considering the computing time, the grid number of this numerical model is about 620 thousands. The average skew of the grids is 0.178, the average orthogonal mass is 0.927, and the average aspect ratio is 2.108. The computer is configured with i5-10400F CPU and RAM16GB for calculation. The CPU running time is 321 minutes, and the residual value is 10^{-5}.

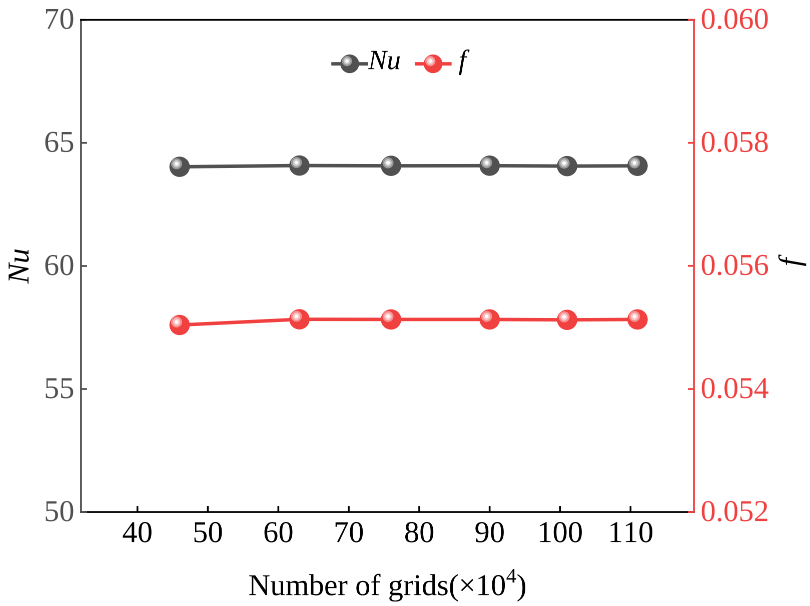

Figure 3. Grid independence verification.

(3) Physical parameters

The fluid medium in the SFCBHE is water. The outer heat conduction tube is made of steel with high thermal conductivity, and the inner insulation tube is made of polyethene, a material with low thermal conductivity. Table 2 shows its physical parameters.

Table 2. Physical parameters of the numerical model.

Parameter	Symbol	Water	Outlet Tube	Inlet Tube	Unit
Density	P	998.2	7850	962	$kg\cdot m^{-3}$
Specific heat capacity	c_ρ	4182	502.48	2630	$J\cdot(kg\cdot K)^{-1}$
Thermal conductivity	k	0.6	44.19	0.02	$W\cdot(m\cdot K)$
Viscosity	M	0.001003	—	—	$kg\cdot(m\cdot s)^{-1}$

2.2.3. Evaluation Indicator

Regarding the enhanced heat transfer, researchers have proposed several evaluation indicators based on the first and second laws of thermodynamics, respectively. Webb [31] et al. presented a comprehensive performance evaluation factor (PEC) integrating the Nusselt number (*Nu*) and friction coefficient (*f*). It can be used to evaluate the overall enhanced heat transfer effect that is influenced by both heat transfer and drag loss of the heat exchanger. It is the most widely applied and used as the evaluation indicator for the performance of heat harvesting. It can be used as the evaluation indicator of the heat extraction performance of SFCBHE. It is expressed as follows:

$$PEC = \frac{(Nu/Nu_s)}{(f/f_s)^{1/3}} \tag{3}$$

where Nu is the Nusselt number for new heat exchangers; f is the friction coefficient of new heat exchangers; Nu_s is the Nusselt number for smooth tubes; and f_s is the friction coefficient of the smooth tube.

When PEC is less than 1, the heat transfer efficiency is low. When PEC is equal to 1, the heat transfer efficiency of the new and smooth tube heat exchangers is the same, and the heat transfer is not enhanced. When PEC is greater than 1, it shows that the comprehensive performance of the new heat exchanger is significantly improved compared with the smooth tube heat exchanger.

2.3. Model Validation

For validating the numerical simulation results, the Nusselt number Nu and the friction factor f of the smooth tube heat exchanger are compared with those obtained by other authors [32–34]. Figure 4 compares the simulation results of the smooth tube heat exchanger with the results of the empirical equations, and the shaded area is the ±6% region of the observed correlations. This demonstrates that the simulation results are within the overlap interval of the two empirical correlations, verifying the numerical model.

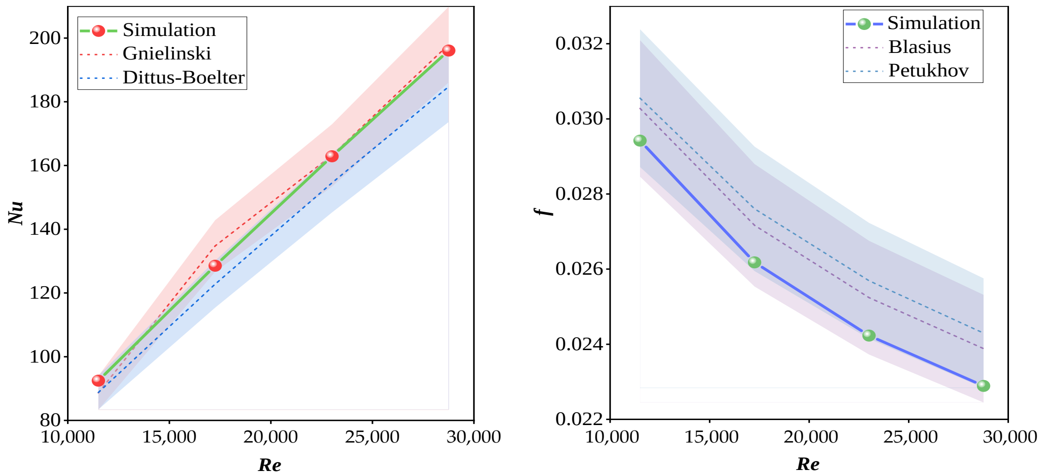

(**a**) Nu result verification (**b**) f result verification

Figure 4. Model validation [19].

2.4. Taguchi Method Program

Another study [27] investigated the fin height and pitch of SFCBHE. It concluded that increasing the fin height or decreasing the pitch of spiral fins can effectively enhance heat extraction performance. Meanwhile, the number of fins, vortex generators, and TDIT also influence the heat extraction performance of the SFCBHE. Therefore, the Taguchi method was used to analyze the effects of fin height H_c, pitch P, number of fins F, the number of vortex generators G (uniform arrangement), and TDIT (H) on heat extraction performance. The calculation results can provide an initial database for the optimization analysis of the heat extraction performance of SFCBHE. According to the fixed parameter dimensions in Table 1 and the range of the fin height and pitch values provided in the literature [27,35,36], the initial values and scopes of the five optimization parameters are determined. Finally, the L16(4^5)Taguchi method test scheme for multi-parameter optimization is formulated. The results of the schemes are calculated using simulation and analysis software. Table 3 presents the test schemes and their corresponding calculation results.

Table 3. Taguchi Method Program and Results.

Levels	Experimental Factors					PEC
	Hc **(mm)**	***P*** **(mm)**	***F*** **(N/A)**	***G*** **(N/A)**	***H*** **(mm)**	
1	5	100	1	1	100	1.036
2	5	200	2	2	300	1.038
3	5	300	3	3	500	1.035
4	5	400	4	4	700	1.012
5	10	100	2	3	700	1.119
6	10	200	1	4	500	1.102
7	10	300	4	1	300	1.042
8	10	400	3	2	100	1.075
9	15	100	3	4	300	1.275
10	15	200	4	3	100	1.224
11	15	300	1	2	700	1.073
12	15	400	2	1	500	1.049
13	20	100	4	2	500	1.314
14	20	200	3	1	700	1.138
15	20	300	2	4	100	1.250
16	20	400	1	3	300	1.155

To verify the representativeness of the optimized parameters, the principal effect analysis of the aforementioned Taguchi method was conducted to investigate the effects of different levels of each factor on the PEC. These results are presented in Figure 5. Here, the more extensive span of the curve indicates that the element is considered to be more representative. The fin height *Hc*, pitch *P*, and the number of vortex generators *G* significantly affect the PEC. The PEC increases with increasing the fin height *Hc* and number of vortex generators *G* and decreases with increasing pitch *P*. The PEC also affects the number of vortex generators *G* and *P*. Therefore, it is representative to use these five influencing factors (fin height *Hc*, pitch *P*, number of fins *F*, number of vortex generators *G* [uniformly arranged], and TDIT (*H*)) to construct the optimization agent model.

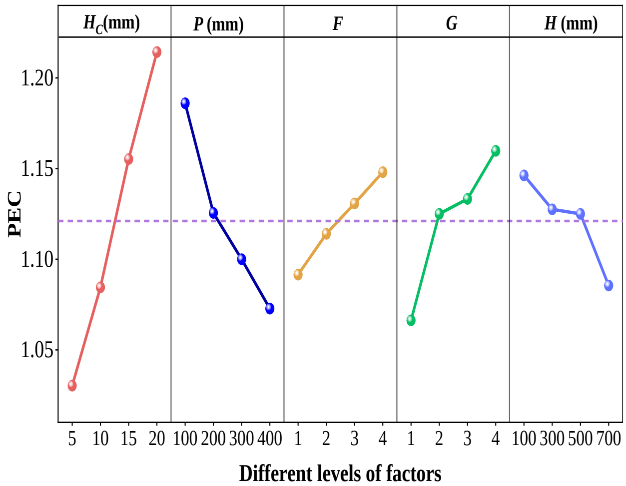

Figure 5. PEC main effects analysis.

3. Optimization Models and Methods

3.1. PEC Optimization Model

For the heat exchanger performance to reach the global optimum level within the optimization interval, it is ensured that all other conditions remain unchanged. Based on the Taguchi method, the fin height H_c, pitch P, and TDIT (*H*) are uniformly varied. The corresponding PEC values are calculated. Finally, a training library of agent models with 135 sets of data is formed. The heat extraction performance of the SFCBHE is optimized using a combination of GA–BPNN and QLMPA. In the optimization model, Hc, P, F, G, and H are the optimization variables; PEC is the optimization objective, and a larger PEC indicates a better heat transfer performance. The optimization model is shown as follows:

$$\begin{aligned} &\max \mathrm{PEC}(X), \\ &X = (Hc, P, F, G, H), \\ &s.t \begin{cases} Hc_{\min} \leq Hc \leq Hc_{\max} \\ P_{\min} \leq P \leq P_{\max} \\ F_{\min} \leq F \leq F_{\max} \\ G_{\min} \leq G \leq G_{\max} \\ H_{\min} \leq H \leq H_{\max} \end{cases} \end{aligned} \tag{4}$$

where ($Hc_{\min}$, $Hc_{\max}$), ($P_{\min}$, $P_{\max}$), ($F_{\min}$, $F_{\max}$), ($G_{\min}$, $G_{\max}$), and ($H_{\min}$, $H_{\max}$) are the constraint intervals for the fin height, pitch, number of fins, number of vortex generators (uniform arrangement), and TDIT(H), respectively.

The decision solution of the optimization model (Equation (4)) is determined by first constructing the mapping relationship model between the comprehensive performance evaluation indicator PEC and the optimization parameters using the GA–BPNN and identifying the parameter optimization model with the maximum PEC as the objective. Then the solution is optimized using QLMPA. Next, the number of fins F and vortex generator G are rounded and substituted into the GA–BPNN model to solve the PEC. The solution flow is shown in Figure 6.

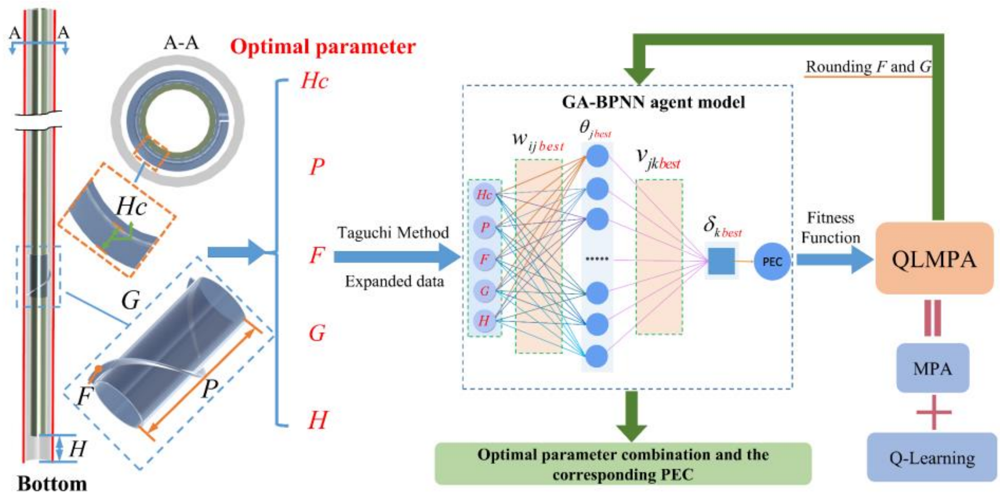

Figure 6. Flowchart of optimized parameters for SFCBHE.

3.2. GA–BPNN Principles and Processes

Using machine learning algorithms allows for establishing an agent model with high accuracy in predicting the PEC value while considering the multifactor nonlinear coupling relationship between the structural size of the SFCBHE and the installation position. The commonly used BPNN for optimization analysis faces the problem of falling into local minima, leading to inaccurate optimization and prediction models. The GA can select crossover and mutation operations on the initial weights and thresholds of BPNN so that the BPNN can get the best initial weights and thresholds, thus improving the prediction model's accuracy. This can effectively address the problem of BPNN falling into local optimum by combining GA and BPNN.

Figure 7 shows the GA–BPNN workflow. First, according to the set network topology, parameters are initialized, the initial weights and thresholds are determined, and the GA structure is identified. Next, the BPNN is trained, and the fitness function is calculated using selection, crossover, and mutation to determine the fitness value until the fitness value meets the end condition to calculate the optimal weights and thresholds. Finally, the weights and thresholds of the BPNN are updated according to the error back-propagation, and the neural network is trained until the end conditions are met. Ultimately, the optimal agent model is obtained.

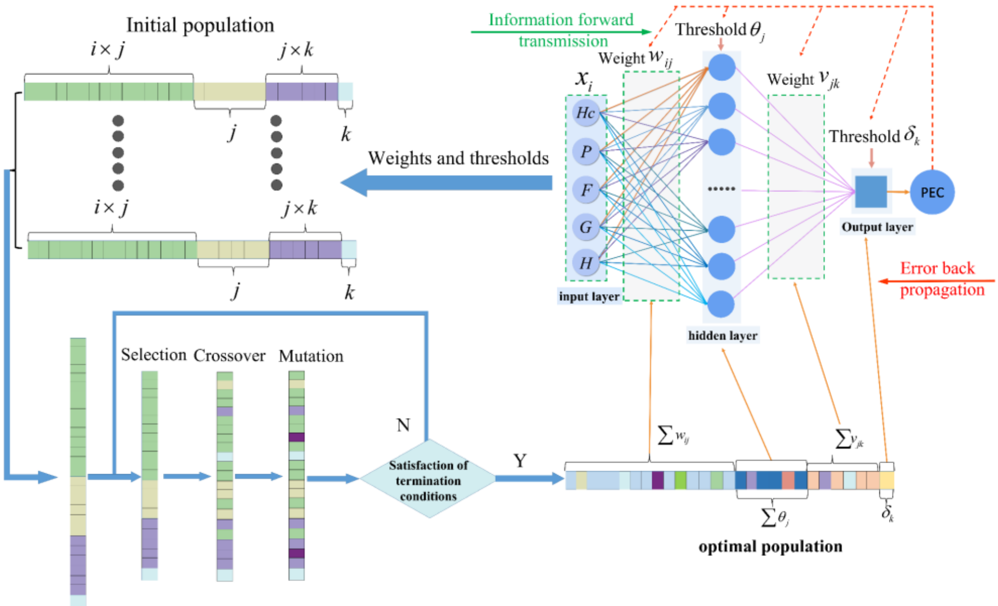

Figure 7. Flowchart of GA–BPNN.

3.3. QLMPA Optimization Principles and Processes

To enhance the heat extraction performance of the SFCBHE, an optimization study of the heat extraction performance of the heat exchanger was conducted using an optimization algorithm based on the GA–BPNN agent model by considering the multifactor nonlinear coupling relationship. The MPA is a swarm intelligence (SI) algorithm proposed by Afshin Faramarzi et al. [37] in recent years, which is inspired by the different foraging strategies among marine predators and the optimal encounter rate strategies in biological interactions, including both Le'vy and Brownian motions [38]. The MPA is uniformly initialized with its solution X^0 on the search space by the following equation:

$$X_{ij}^0 = r_{ij}(ub_j - lb_j) + lb_j, \quad i = 1, \ldots, n \quad j = 1, \ldots, d \tag{5}$$

where X_{ij}^0 is the element of the *i*th row and *j*th column of matrix X^0; ub_j and lb_j are the upper and lower limits of the range of values of each optimization parameter in Table 1. r_{ij} is a uniform random number between 0 and 1; n is the total number of search agents; and d is the dimensionality of the solution, denoted as the number of optimization parameters.

In marine ecosystems, both predators and prey are considered search agents, and the best of them is considered *Elite* with the expression:

$$Elite = \begin{bmatrix} X_{1,1}^I & X_{1,2}^I & \cdots & X_{1,d}^I \\ X_{2,1}^I & X_{2,2}^I & \cdots & X_{2,d}^I \\ \vdots & \vdots & \vdots & \vdots \\ X_{n,1}^I & X_{n,2}^I & \vdots & X_{n,d}^I \end{bmatrix}_{n \times d} \tag{6}$$

The others are called *Prey*, and their proxy matrices are of the same dimension as *Elite*, shown by the following expression:

$$Pery = \begin{bmatrix} X_{1,1} & X_{1,2} & \cdots & X_{1,d} \\ X_{2,1} & X_{2,2} & \cdots & X_{2,d} \\ \vdots & \vdots & \vdots & \vdots \\ X_{n,1} & X_{n,2} & \cdots & X_{n,d} \end{bmatrix}_{n \times d} \tag{7}$$

MPA selects the appropriated motion based on the relationship between the number of iterations and the maximum number of iterations and does not utilize the information generated from previous iterations, increasing the computational cost and running time and reducing the convergence speed to address this shortcoming. The use of reinforcement learning Q-learning to fully use the iteration information can improve the convergence speed of MPA and avoid prematurely falling into the development phase [26]. In the Q-learning algorithm, the Q-table is updated according to the Bellman equation (Equation (8)) to gain experience.

$$Q(s^{Iter+1}, a^{Iter+1}) = Q(s^{Iter}, a^{Iter}) + \lambda \left[r_{Iter+1} + \gamma \max_{a}(Q(s', a)) - Q(s^{Iter}, a^{Iter}) \right] \tag{8}$$

where λ is the learning rate, γ is the discount factor between 0~1, and r_{Iter+1} is the instant reward calculated by s^{Iter} and a^{Iter}.

Based on the GA–BPNN agent model and QLMPA optimization principle, combined with the optimization objective (maximum PEC) and optimization variables (*Hc*, *P*, *F*, *G*, and *H*), the workflow is shown in Figure 8. The specific process can be divided into the following steps:

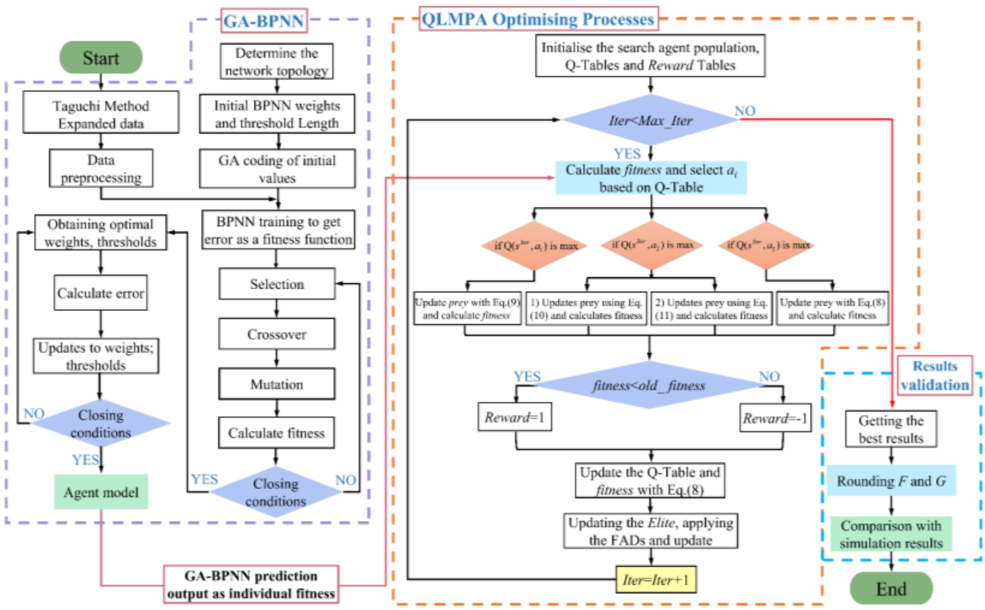

Figure 8. Optimization flowchart of GA–BPNN–QLMPA.

(1) Initialize the search agent ($Prey_i$) population i = 1,. . ., n, Q-table, and Reward table, as well as the current state s^0;

(2) When the number of iterations is less than the maximum, the trained GA–BPNN prediction output is used as *old_fitness*. The *Elite* matrix is constructed;

(3) If Q(S^{Iter},a_1) is the maximum value in the Q-table, which is the initial phase of optimization, the predator moves faster than the prey, and *Prey* is updated using the following equation:

$$\begin{aligned} &\overrightarrow{stepsize_i} = \overrightarrow{R_B} \otimes \left(\overrightarrow{Elite_i} - \overrightarrow{R_B} \otimes \overrightarrow{Prey_i}\right) \quad i = 1, \ldots, n \\ &\overrightarrow{Prey_i} = \overrightarrow{Prey_i} + P \cdot \overrightarrow{R} \otimes \overrightarrow{stepsize_i} \end{aligned} \tag{9}$$

where R_B is a vector of random numbers containing the Brownian motion normal distribution; the symbol ⊗ denotes term-by-term multiplication; P is a constant, taken as 0.5; and R is a vector of uniform random numbers in the interval 0~1.

(4) If Q(S^{Iter},a_2) is the maximum value in the Q-table, this is an optimized intermediate stage where the predator moves at a speed equal to the prey, and the setting is designed to be half for exploration and half for exploitation. For the exploration part of the population, *Prey* is updated according to Equation (10);

$$\begin{aligned} &\overrightarrow{stepsize}_i = \overrightarrow{R_L} \otimes \left(\overrightarrow{Elite}_i - \overrightarrow{R_L} \otimes \overrightarrow{Prey_i}\right) \quad i = 1, \ldots, n/2 \\ &\overrightarrow{Prey_i} = \overrightarrow{Prey_i} + P \cdot \overrightarrow{R} \otimes \overrightarrow{stepsize_i} \end{aligned} \tag{10}$$

where R_L is a vector of random numbers with Le'vy distribution.
For another part of the population, *Prey* is updated according to the following equation:

$$\begin{aligned} &\overrightarrow{stepsize}_i = \overrightarrow{R_B} \otimes \left(\overrightarrow{R_B} \otimes \overrightarrow{Elite}_i - \overrightarrow{Prey_i}\right) \quad i = n/2+1, \ldots, n \\ &CF = \left(1 - \frac{Iter}{Max\_Iter}\right)^{\left(2\frac{Iter}{Max\_Iter}\right)} \\ &\overrightarrow{Prey_i} = \overrightarrow{Elite}_i + P \cdot CF \otimes \overrightarrow{stepsize_i} \end{aligned} \tag{11}$$

where $\overrightarrow{R_B} \otimes \overrightarrow{Elite}_i$ simulates the Brownian motion of the predator; and CF is an adaptive parameter to control the step size of the predator.

(5) If Q(S^{Iter},a_3) is the maximum value in the Q-table, this is the final stage of optimization, and *Prey* is updated using the following equation:

$$\begin{aligned} &\overrightarrow{stepsize}_i = \overrightarrow{R_L} \otimes \left(\overrightarrow{R_L} \otimes \overrightarrow{Elite}_i - \overrightarrow{Prey_i}\right) \quad i = 1, \ldots, n \\ &\overrightarrow{Prey_i} = \overrightarrow{Elite}_i + 0.5CF \otimes \overrightarrow{stepsize_i} \end{aligned} \tag{12}$$

where $\overrightarrow{R_L} \otimes \overrightarrow{Elite}_i$ simulates the predator Lev'y flight motion. Other factors influence the predator behavior, with eddy currents and fish aggregating devices (FADs) effects being the most significant [39,40].

(6) Calculate *fitness* based on *Prey*; if *fitness* < *old_fitness*, *Reward* = 1, otherwise, *Reward* = −1;

(7) Update the Q-table with Equation (8), complete the *Elite* update, apply the FADs effect and update;

(8) Add one to the number of iterations and go back to step 2;

(9) At the end of the iteration, the best fitness and its corresponding *Prey* are returned. *fitness* is the optimal PEC obtained with QLMPA, and *Prey* is the optimal value of SFCBHE optimization variables (*Hc*, *P*, *F*, *G*, *H*);

(10) The number of fins *F* and the number of vortex generators *G* in the optimal optimization variables obtained in step 9 are circularly substituted into the trained PEC agent model to find the PEC values;

(11) Compare the results of the parameter combinations obtained in step 10 with the simulation analysis results to evaluate the optimized model's accuracy.

4. PEC Prediction Model and Optimization Analysis

4.1. PEC Prediction Model

The PEC prediction model is built using GA–BPNN, and the model sample data are 135 sets. The training, validation, and test sets are selected using random sampling. Moreover, the training set: the validation set: the test set = 0.7:0.15:0.15. The data are normalized using the min-max normalization method to reduce the error. The input layer of the BPNN is the fin height *Hc*, screw pitch *P*, number of fins *F*, number of vortex generators *G*, TDIT (*H*). The output layer is the PEC value. The GA and BPNN parameters are presented in Table 4.

Table 4. Parameters of GA–BPNN.

Parameter	Symbol	Value
GA	Population size	10
	Number of iterations	30
	Crossover probability	0.8
	Probability of variation	0.2
BPNN	Input Variables	5
	Number of hidden layers	1
	Number of neurons in the hidden layer	10
	Maximum number of iterations	1000
	Learning rate	0.01
	Precision	0.0001

The fitness curve describes the process of finding the optimal weights and thresholds of BPNN by GA, including the average fitness and the best fitness curve (Figure 9). The average adaptation tends to decrease with the number of iterations. The optimal fitness value reaches stability at 23 iterations, which is 6.25×10^{-4}. The PEC prediction model can be built by substituting the initial weight threshold under the optimal fitness into the BPNN.

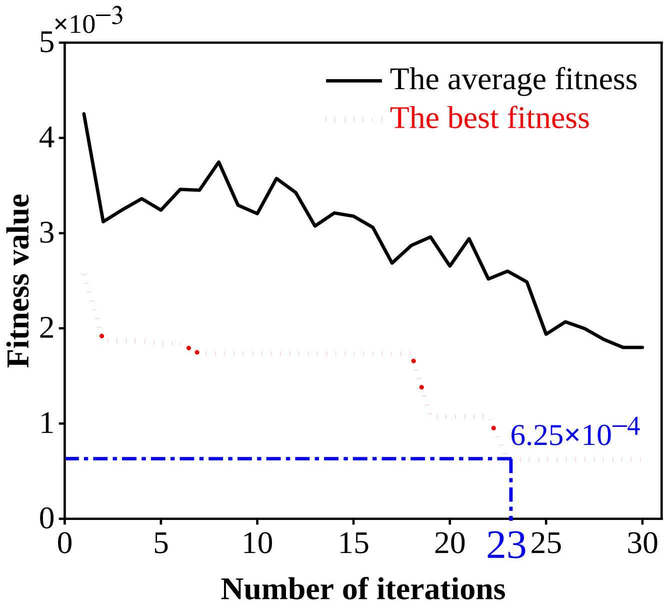

Figure 9. Adaptation curve of each output parameter of GA–BPNN.

Model prediction accuracy is a prerequisite for accurately evaluating the heat transfer performance of SFCBHE. Both test set's prediction accuracy and error analysis are investigated to obtain a high-precision prediction model.

(1) Test set prediction accuracy

The test set prediction accuracy directly affects the model accuracy. Figure 10 depicts the GA–BPNN prediction results, in which the mauve dots are the data points determined according to the PEC prediction model with the simulation value as the coordinates. The red straight line indicates the zero error line, and the blue dashed line indicates the +5% upper limit and –5% lower limit of the error. The blue data points fluctuate around the zero error line and are within upper and lower error limits. The histogram of the frequency distribution of the relative errors of the PEC prediction model is depicted in the lower right corner. The green line is the Gaussian fitting curve, representing the relationship between the relative errors and the frequencies. The relative error is 90% between ±1.5% and 10% between −3.5% and −2.5%. Together, they validate the accuracy of the PEC prediction model.

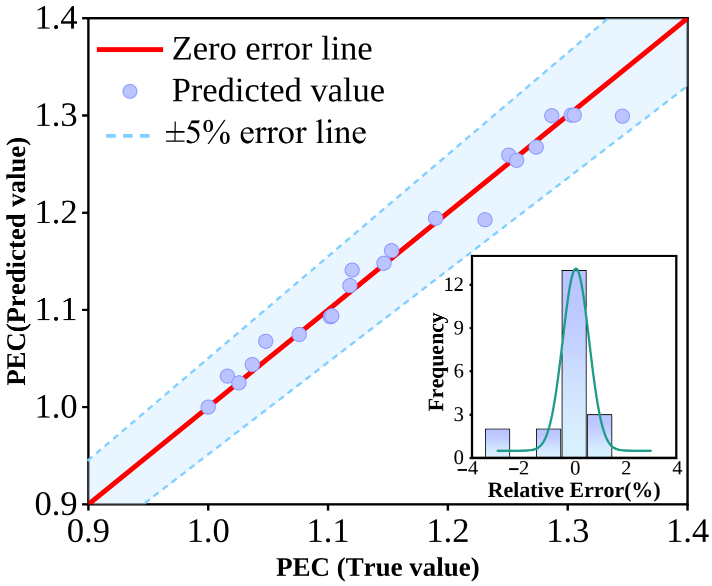

Figure 10. Results of GA–BPNN prediction.

(2) Error analysis

The superiority of the PEC prediction model is evaluated by comparing it with the BPNN and SVR models, commonly used in the existing literature. The relative error of each model concerning the simulation results is taken as the absolute value using the simulation results as the benchmark. The results are shown in Figure 11. In BPNN and SVR, compared to GA–BPNN, the lower contour map is darker in color, and the upper 3D peak map has steeper wave crests. The absolute value of the maximum relative error of BPNN and SVR models is 7.23% and 15.11%, respectively. In contrast, the absolute value of the maximum relative error of the GA–BPNN model is 3.44%, indicating that the PEC prediction model established by GA–BPNN predicts the training set more accurately.

To further evaluate the prediction effect of GA–BPNN, BPNN, and SVR models, the mean square error (MSE), mean absolute percentage error (MAPE), and goodness of fit (R^2) are used as the evaluation indicators of prediction accuracy. The smaller the values of MSE and MAPE, the closer the predicted value is to the actual value. The closer R^2 is to 1, the more accurately the model describes the mapping between the inputs and outputs. The expressions of the three evaluation indicators are as follows:

$$MSE = \frac{1}{m}\sum_{\mathrm{i}=1}^{\mathrm{m}}(P(i) - y(i))^2 \tag{13}$$

$$MAPE = \frac{1}{m}\sum_{i=1}^{m}\left|\frac{P(i)-y(i)}{y(i)}\right| \tag{14}$$

$$R^2 = \sum_{i=1}^{m}(P(i)-y(i))^2 \Bigg/ \sum_{i=1}^{m}(\overline{y}-y(i))^2 \tag{15}$$

where $P(i)$ is the predicted value of the ith test sample; $y(i)$ is the measured value of the ith test sample; $\overline{y}$ is the average of the measured values; and m is the number of test samples.

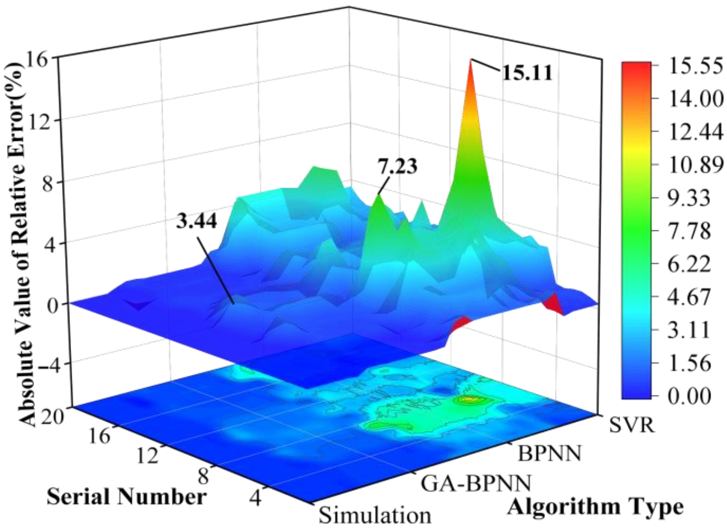

Figure 11. Comparison of the prediction accuracy of the three models.

The comparison of the prediction results of the three models is shown in Figure 12, which shows that the MSE and MAPE of the GA–BPNN model are smaller than that of the BPNN and SVR. The R^2 reaches 0.9611, which is 11.28% and 8.96% higher than that of the BPNN and SVR, respectively. The results demonstrate that the PEC prediction model obtained using GA–BPNN has more precision.

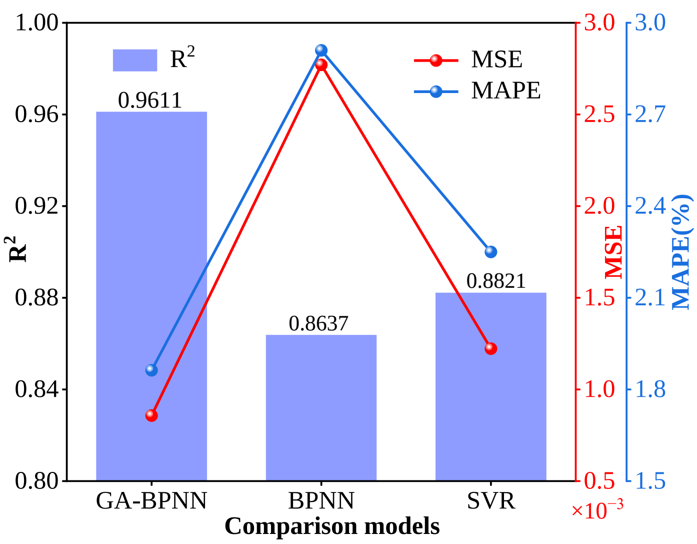

Figure 12. Comparison of three model predictions.

In summary, the PEC prediction model constructed using GA–BPNN has high accuracy obtained by studying the test set prediction accuracy and error analysis.

4.2. PEC Optimization Analysis

4.2.1. SFCBHE Parameter Optimization Results

Constructing a high-precision PEC prediction model using GA–BPNN is the foundation for optimizing the heat extraction performance of SFCBHE. Furthermore, iterative optimization using QLMPA with the GA–BPNN prediction output as the adaptation value is the key to this optimization. The QLMPA parameters are determined by the grid search method and in combination with the literature [26], and the specific parameters are shown in Table 5.

Table 5. QLMPA parameter setting.

Parameter	Symbol	Value
Discount factor	γ	0.5
Learning rates	λ	0.01
FADs	N/A	0.2
Step size factors	P	0.5
Number of iterations	I	500
Search agent	N/A	25
Discount factor	γ	0.5

The PEC results satisfying the optimization model (Equation (4)) are obtained using QLMPA and are shown in Figure 13. The horizontal coordinate is the number of iterations, and the vertical coordinate is the optimal PEC value corresponding to each iteration. The optimal PEC increases with the increase in the number of iterations, and the fastest rise of PEC is observed when the number of iterations is in 0~4. When the number of iterations is in the interval of 5~45, the PEC shows a stepwise increase. When the number of iterations is 45, it has already reached the globally optimal PEC value, which is attributed to the fact that the Q-learning algorithm fully use iterative information, making the exploration and development phase of MPA more effective and improving the convergence speed of MPA. The maximum value of PEC is 1.423, and its corresponding heat exchanger structural parameters are Hc = 20.00 mm, P = 100.00 mm, F = 4, G = 3.45, and H = 408.5 mm.

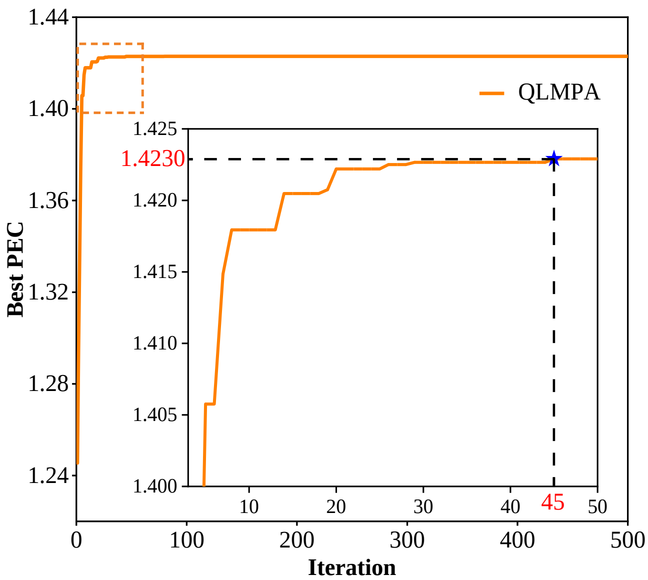

Figure 13. Iterative optimization process of QLMPA.

4.2.2. QLMPA Optimization Performance Evaluation

For evaluating the performance of QLMPA on the optimization problem of heat extraction performance of SFCBHE, QLMPA is compared with several optimization algorithms most commonly used in the current literature, such as the MPA algorithm (MPA), grey wolf optimization algorithm (GWO), and particle swarm algorithm (PSO). Table 6 presents the parameter settings for MPA, GWO, and PSO.

Table 6. Parameter settings for MPA, GWO, and PSO.

MPA		GWO		PSO	
Parameter	**Value**	**Parameter**	**Value**	**Parameter**	**Value**
FADs	0.2	Dimension	5	Population size	50
Step size factors	0.5	Number of Iterations	500	Dimension	5
Number of Iterations	500	Search Agent	25	Acceleration constant	0.2
FADs	0.2	Dimension	5	Population size	50

The optimal PEC value obtained by each algorithm and the number of iterations (I_{best}) to bring the optimal PEC value are used as evaluation indicators, wherein the more significant the PEC indicates, the better the optimization effect. Moreover, the smaller the number of iterations (I_{best}), the higher the optimization efficiency.

Figure 14 shows the variation of the optimal PEC with the number of iterations for each optimization algorithm. Table 7 presents the parameter combinations of the SFCBHE calculated by each optimization algorithm and the corresponding PEC and I_{best}. Figure 14 and Table 7 demonstrate that the QLMPA, MPA, and GWO algorithms obtain the exact optimal PEC through iterations. The local zoom in Figure 14a shows that QLMPA converges faster than MPA and GWO in 0–100 iterations, which is due to the fact that MPAs can store information about the searches that they have obtained throughout the iteration process with the help of Q-learning, making the exploration and development phases of MPA more effective and improving the convergence speed of MPA. The local zoom in Figure 14b shows that QLMPA has reached the optimal value in 45 iterations, and the computational speed is 33.8%, 47.7%, and 31.8% higher than that of MPA, GWO, and PSO, respectively. Therefore, QLMPA can be used to quickly calculate the optimal SFCBHE parameter combinations and significantly enhance the design efficiency.

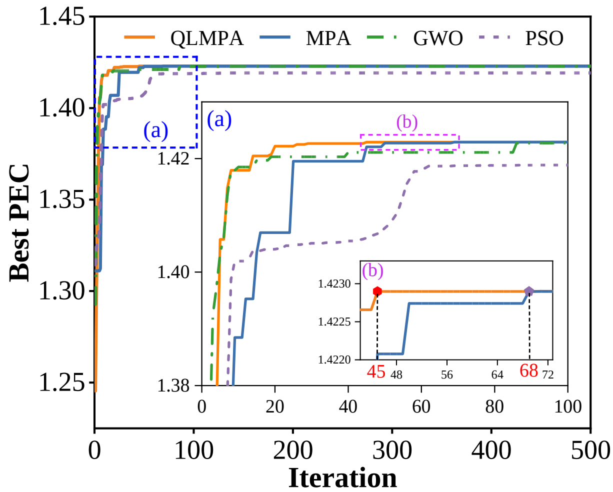

Figure 14. Iteration optimization process comparison of the algorithms. (**a**) Locally enlarged image of iteration of the algorithms; (**b**) Locally enlarged image of iteration of QLMPA and MPA.

Table 7. Best parameter combinations for each optimization algorithm.

Type	Hc	P	F	G	H	PEC	I_{best}
QLMPA	20	100	4	3.45	408.5	1.423	45
MPA	20	100	4	3.45	408.5	1.423	68
GWO	20	100	4	3.45	408.5	1.423	86
PSO	19.5	100	3.83	4	294.9	1.419	66

The number of vortex generators G obtained from QLMPA was rounded to 3 and 4. It was then substituted into the PEC prediction model, simulation, and analysis software. The results are shown in Figure 15. The best PEC value is obtained from the simulation and GA–BPNN model when the number of vortex generators is 4, and the relative error is only –0.58%. Therefore, the optimal parameter combination is H_c = 20 mm, P = 100 mm, F = 4, G = 4, and H = 408.5 mm.

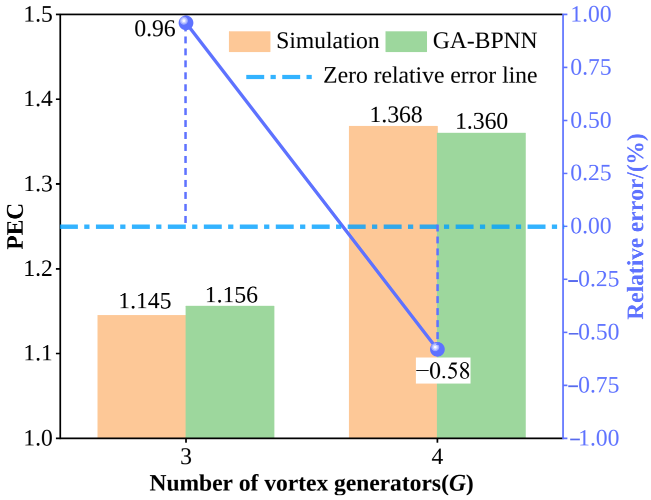

Figure 15. Comparison of the number of vortex generators.

5. Optimized SFCBHE Heat Extraction Analysis

5.1. Heat Extraction Performance Comparison before and after Optimization

For the analysis of the PEC enhancement effect after optimization, the smooth pipe TY-1 structure is widely used in engineering practice. The TY-2 structure before optimization (considering the single-factor optimization of SFCBHE) and the TY-3 structure obtained by considering the multifactorial coupling effect are compared. Table 8 presents the structural parameters of each scheme and the corresponding PEC values. According to the data in Table 8, the structural diagrams of the three schemes is obtained as shown in Figure 16, where H1 = H2 = 300 mm and H3 = 408.5 mm.

Table 8. Comparison of three structures.

Type	Hc	P	F	G	H	PEC
Unit	mm	mm	pieces	pieces	mm	N/A
TY-1	–	–	–	–	300	1.04
TY-2	15	300	1	1	300	1.10
TY-3	20	100	4	4	408.5	1.36

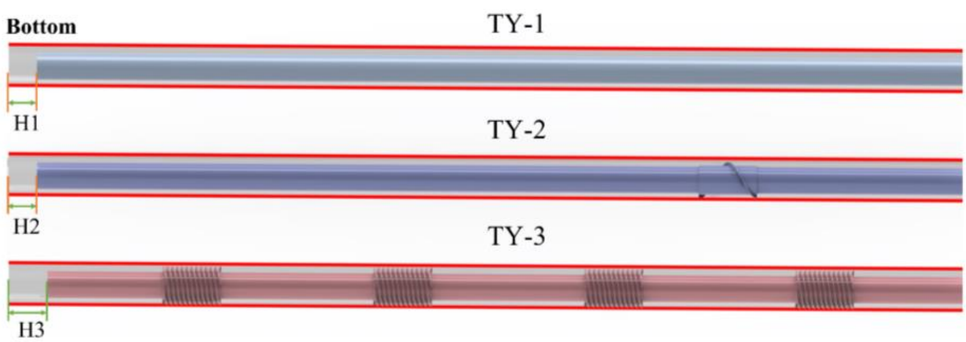

Figure 16. Comparison of the appearance of the three structures.

As shown in Figure 17, it is the distribution of turbulent kinetic energy in the vortex generator segment of the three different structures TY-1, TY-2 and TY-3. Figure 17 shows that the turbulent kinetic energy of structure TY-3 is the strongest, that of structure TY-2 is the second, and that of structure TY-1 is the weakest. The introduction of vortex generator reduces the cross-sectional area of the flow channel and increases the flow velocity. Moreover, the fins on the vortex generator make the fluid move from a straight line to a spiral motion, which produces a guiding and shearing effect on the fluid. As a result, the disturbance characteristics of the fluid are enhanced. Compared with structure TY-2, the number of fins F and fin height H_c of structure TY-3 are larger, which results in a larger increase of the flow velocity and turbulent kinetic energy. Therefore, the structure of TY-3 is more conducive to geothermal exploitation.

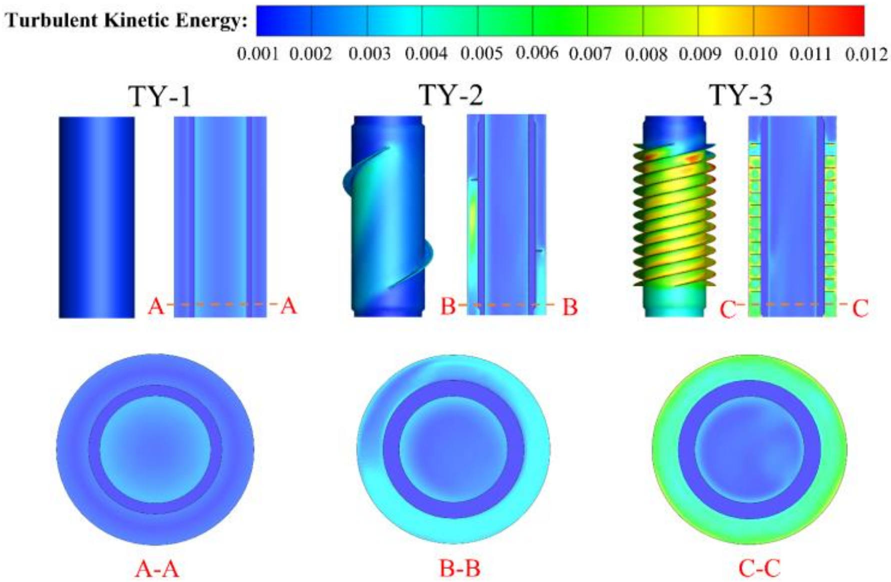

Figure 17. Distribution of turbulent kinetic energy in vortex generator segment of three different structures TY-1, TY-2 and TY-3.

To investigate the temperature distribution of the SFCBHE by the structural differences before and after optimizing, the simulation analysis was performed for the three structures of TY-1, TY-2, and TY-3. The longitudinal sectional temperature distribution of the three structures was obtained, as shown in Figure 18a. The guidance and shearing effect of the vortex generator on the fluid changes the flow direction and flow velocity. The spiral flow is formed and prolong the heat transfer path between fluid and high-temperature wall. Meanwhile, the decrease of the cross-sectional area increases the average flow velocity of the cross-sectional fluid and strengthens the disturbance performance of the fluid. Furthermore, the boundary layer destruction of the high temperature wall is stronger, and the mixing effect of the high temperature fluid and the low temperature fluid is better. As a result, a better heat exchange effect between the fluid and the high temperature wall is obtained. As shown in Figure 18a, the fluid temperature in the annulus of structure TY-2 and TY-3 increases significantly.

Figure 18b is the cross-section temperature distribution of structure TY-3. It can be seen from the figure that the fluid flows from the annular inlet of the heat exchanger to the bottom of the well, the temperature rises rapidly, and the temperature stays basically unchanged after flowing into the insulation pipe. This suggests that the insulation pipe has better insulation performance.

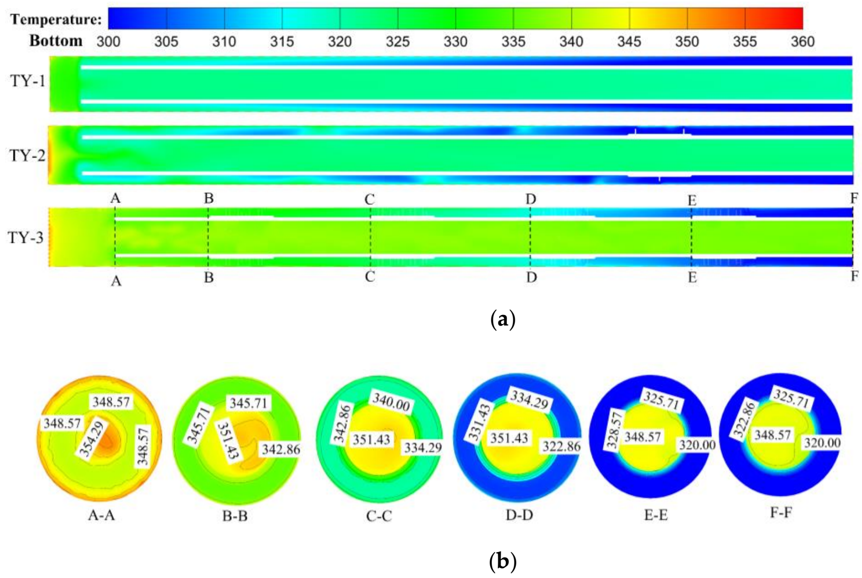

Figure 18. Temperature distribution cloud of three structures. (**a**) Temperature distribution cloud diagrams of longitudinal sections of three structures; (**b**) cross-section temperature distribution of structure TY-3.

Figure 19 shows the temperature distribution curves along the radial direction for six cross-sections from A-A to F-F. The figure shows that the fluid temperature near the high temperature wall is higher. Since the thermal conductivity of the fluid is small, the temperature of the fluid away from the high temperature wall drops sharply. The thermal is not transferred to the center of the fluid, and the temperature of the fluid in the center area is basically the same. As the fluid moves along the flow direction, from inlet cross section F-F to bottom hole cross section A-A, the average fluid temperature increases from 300K to 350K. Figure 19 also shows that the fluid outlet temperature in the insulation tube is about 349K, 49K higher than the inlet temperature, and the lift rate is 16.3%.

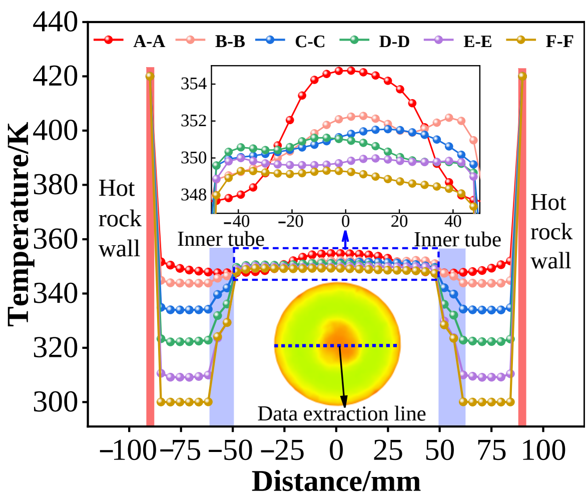

Figure 19. Temperature comparison of six groups of cross-sections for structure TY-3.

Figure 20 shows the velocity distribution and 2D and 3D flow maps of the annulus region extracted from the three structures TY-1, TY-2, and TY-3 at the positions of 1 m, 3.67 m, 6.33 m, and 9 m from the bottom of the well, respectively. The flow lines in the annulus of the TY-1 smooth tube are linear, and the perturbation characteristics are not prominent. However, the cross-sectional flow line figure shows that the annulus fluid is also perturbed under turbulence. Compared with the TY-1, TY-2 with a vortex generator, the flow line shows a spiral shape after the fluid passes through the vortex generator, the turbulent kinetic energy of the fluid increases. Meanwhile, the spiral flow prolongs the heat conduction time between the fluid and the hot wall surface, which is conducive to improving the geothermal mining effect. The cross-sectional velocity cloud and streamline figures show that the fluid is spinning better. The flow perturbation characteristics are enhanced to improve the mixing effect of the hot fluid near the wall and the cold fluid inside, strengthening the flow heat transfer effect. Compared with TY-2, the number of vortex generators in TY-3 is increased, the turbulent kinetic energy of the fluid is further strengthened, so that the cyclonic intensity of the fluid in the annulus is significantly higher than that of the TY-2 structure. The thermal conductivity path of the fluid is also considerably enhanced, which is conducive to absorbing more heat from the hot rock wall. The cross-section cloud diagram and flow line figures demonstrate that the cyclonic intensity of TY-3 is more noticeable or significant. The perturbation effect of the fluid is the best. In conclusion, the optimized TY-3 exhibits a better heat transfer effect and is more suitable for geothermal energy extraction.

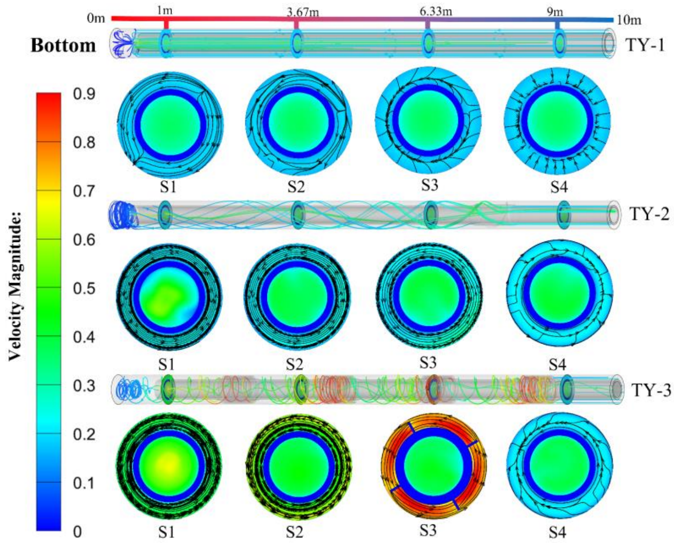

Figure 20. Three-dimensional and cross−sectional velocity streamlines variation for the three structures.

5.2. Heating Effect Assessment before and after Optimization

The heat extraction capability of the SFCBHE is primarily evaluated in terms of heat extraction temperature and heat extraction power. Among other things, the heat extraction power Q_{out} is affected by the physical parameters of the fluid, the size of the flow channel, the flow velocity of the extracted fluid, and the temperature difference between the inlet and outlet, which is expressed as follows [41,42]:

$$Q_{out} = c_\rho \rho A_r V_{out}(T_{out} - T_{in}) \tag{16}$$

where c_ρ is the specific heat capacity of water, J/(kg·k); ρ is the density of water, kg/m^3; A_r is the production well flow area, m^2; V_{out} is the extracted fluid flow velocity, m/s; T_{out} is the extraction temperature, K; and T_{in} is the injection temperature, K.

Figure 21 shows the variation of extracted water temperature for the three heat exchanger configurations at different flow velocities. I-1 and I-2 indicate the elevated temperature of TY-3 relative to TY-1 and TY-2 at different flow velocities, respectively. Since the vortex generator brings stronger disturbance to the flow field, it leads to stronger boundary layer effect and fluid mixing effect. Therefore, as shown in the column diagram in Figure 21, the extracted water temperature of TY-3 and TY-2 is higher than that of TY-1. Compared with TY-2, the extracted water temperature of TY-3 is significantly higher, indicating that TY-3 has better thermal recovery performance and is more suitable for geothermal mining. With the increase of inlet flow velocity, the increase of turbulent kinetic energy is conducive to heat transfer. But the mass flow velocity of low-temperature fluid increases as well, and the temperature rise rate slows down. Then when the heat transfer increment caused by the increase of flow velocity cannot meet the energy required by the temperature rise of more low-temperature fluid, the extracted water temperature presents a slow downward trend. The curves in Figure 21 shows that the temperature lift rate of TY-3 firstly increases and then decreases with the increase of inlet flow velocity. The maximum fluid temperature is obtained when the inlet velocity is 0.2 m/s.

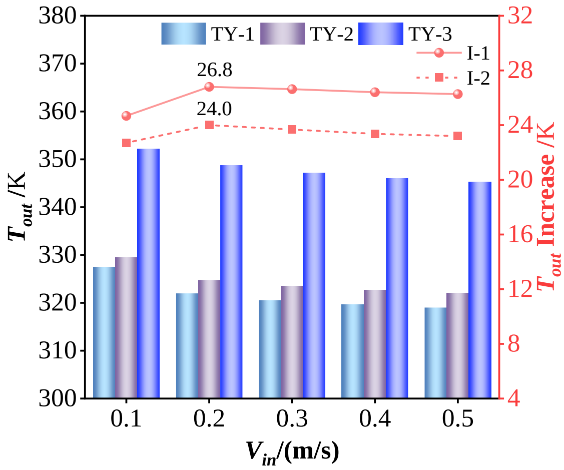

Figure 21. Water temperature changes of three heat exchangers at different flow velocities.

Figure 22 shows the variation curves of heat extraction power with flow velocity for the three heat exchangers. L-1 and L-2 denote the enhancement rate of heat extraction power of TY-3 relative to TY-1 and TY-2 at different flow velocities, respectively. As shown in the column diagram in Figure 22, TY-3 has the highest heat extraction power at the same flow velocity. When the inlet flow velocity increases, the flow rate of low temperature fluid increases and the temperature rise rate slows down. Then, the temperature difference between the fluid and the high temperature wall becomes larger, and the turbulence characteristics are enhanced. It is conducive to the heat transfer performance between the fluid and the wall, and finally the heat extraction power is gradually increased. As shown in the curves in Figure 22, with the increase of inlet flow velocity, the fluid flow rate increases. More energy can be absorbed from the high temperature wall by the fluid, then the heat extraction power increases. But with the increase of inlet flow velocity, the flow rate of lower temperature fluid increases as well, so the rate of increase rate gradually decreases. When the inlet flow velocity is 0.5 m/s, the thermal extraction power of TY-1, TY-2 and TY-3 is 41.4 kW, 49.1 kW and 102.8 kW, respectively. Compared with the thermal recovery power of TY-1, the thermal recovery power of TY-2 is increased by 109.5%, and the thermal recovery power of TY-3 is increased by 148.2%.

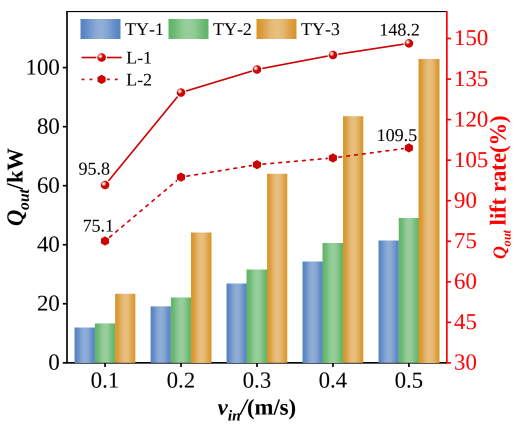

Figure 22. Variation of heat extraction power of three heat exchangers at different flow velocities.

6. Conclusions

The heat extraction performance is optimized by combining GA–BPNN and QLMPA algorithms to improve the geothermal energy extraction efficiency while considering the multifactorial coupling effects of structural size and installation position of the SFCBHE. The primary conclusions of this study are as follows:

(1) Orthogonal test and principal effect analysis were used to analyze the influence of main structural parameters on PEC. The results show that the degree of their influences was as follows: the fin height Hc > pitch P > number of vortex generators G > the distance of the lower end of the inlet tube from the bottom of the well H > number of fins F.

(2) The PEC prediction model is constructed using GA–BPNN, its prediction accuracy is 96.11%, which is 11.28% and 8.96% higher than that of the BPNN and SVR, respectively.

(3) A fast design method is proposed for the SFCBHE based on the intelligence algorithm GA-BPNN-QLMPA. The PEC of the optimized SFCBHE is 1.36, it has been enhanced by 30.8% compared with traditional CBHE. The heat recovery performance of the optimized SFCBHE has been greatly improved.

(4) When the flow rate is 0.2 m/s, the optimized SFCBHE has the highest extracted temperature, which is increased by 26.8 K compared to the smooth tube and 24.0 K compared to the pre-optimized SFCBHE. When the flow rate is 0.5 m/s, the optimized SFCBHE has the highest extracted power 102.8 kW, which is increased by 148.2% and 109.5% compared to the smooth pipe and the pre-optimized SFCBHE, respectively. Therefore, it is crucial to consider the extraction temperature and heat extraction power to determine the injection flow rate to achieve the optimal heat extraction.

Author Contributions: Conceptualization, B.F. and J.Y.; Formal analysis, Z.G. and L.S.; Investigation, L.S.; Methodology, B.F., Z.G. and J.Y.; Software, Z.G. and L.N.; Validation, J.Y. and S.Z.; Writing—original draft, B.F. and Z.G.; Writing—review & editing, B.F. and S.Z. All authors have read and agreed to the published version of the manuscript.

Funding: This research was funded by the Open Foundation of Cooperative Innovation Center of Unconventional Oil and Gas, Yangtze University (Ministry of Education & Hubei Province), No. UOG2022-29 and the Science Research Program of Hubei Provincial Department of Education, grant number D20221304.

Data Availability Statement: The data presented in this study are available on request from the corresponding author. The data are not publicly available due to privacy.

Acknowledgments: We express our gratitude to the anonymous reviewers for their invaluable insights and constructive feedback.

Conflicts of Interest: The authors declare no conflict of interest.

Nomenclature

SFCBHE	Spiral fin coaxial borehole heat exchanger
PEC	performance evaluation factor
GA-BPNN	gen-etic algorithm–back-propagation neural network
QLMPA	Q-learning-based marine predator algorithm
CBHE	coaxial borehole heat exchanger
BHE	borehole heat exchanger
DOTVG	the distance of the vortex generator from the bottom of the inner tube
TL	the total length of SFCBHE
OTD	the outer tube diameter
ITI	the insulation tube inner diameter
TVGD	the vortex generator's diameter
T_W	the rock temperature, K
T_{sur}	the ground surface temperature, K

T_g	the land temperature gradient, K/m
z	the well depth, m
H_c	fin height
P	pitch
F	number of fins
G	the number of vortex generators (uniform arrangement)
TDIT(H)	the distance of the lower end of the inlet tube from the bottom of the well
TY-1	the smooth pipe structure
TY-2	The structure of considering the single-factor optimization of SFCBHE
TY-3	the structure obtained by considering the multifactorial coupling effect
I-1	the elevated temperature of TY-3 relative to TY-1
I-2	the elevated temperature of TY-3 relative to TY-2
L-1	the enhancement rate of heat extraction power of TY-3 relative to TY-1
L-2	the enhancement rate of heat extraction power of TY-3 relative to TY-2

References

1. Rohit, R.V.; Kiplangat, D.C.; Veena, R.; Jose, R.; Pradeepkumar, A.P.; Kumar, K.S. Tracing the evolution and charting the future of geothermal energy research and development. *Renew. Sustain. Energy Rev.* **2023**, *184*, 113531.
2. Dincer, I.; Rosen, M.A. *Exergy Analysis of Heating, Refrigerating and Air Conditioning: Methods and Applications*; Elsevier: Amsterdam, The Netherlands, 2015.
3. Dor, J.; Wang, G.L.; Zheng, K.Y. *Study on the Development and Utilization Strategy of Geothermal Resources in China*; Science Press: Beijing, China, 2017.
4. Dor, J. The basic characteristics of the Yangbajing geothermal field—A typical high temperature geothermal system. *Eng. Sci.* **2003**, *5*, 42.
5. Cao, R.; Dor, J.; Li, Y.; Meng, H.; Cai, Y. Occurrence characteristics, development status, and prospect of deep high-temperature geothermal resources in China. *Chin. J. Eng.* **2022**, *44*, 1623–1631. [CrossRef]
6. Dai, C.; Li, J.; Shi, Y.; Zeng, L.; Lei, H. An experiment on heat extraction from a deep geothermal well using a downhole coaxial open loop design. *Appl. Energy* **2019**, *252*, 113447. [CrossRef]
7. Huang, Y. Research on Heat Transfer Mechanism and Thermal Reservoir Enhancement of Deep Coaxial Borehole Heat Exchanger in Cold Region. Ph.D. Thesis, Jilin University, Jilin, China, 2021. [CrossRef]
8. Holmberg, H.; Acuña, J.; Næss, E.; Sønju, O.K. Thermal evaluation of coaxial deep borehole heat exchangers. *Renew. Energy* **2016**, *97*, 65–76. [CrossRef]
9. Beier, R.A.; Acuña, J.; Mogensen, P.; Palm, B. Transient heat transfer in a coaxial borehole heat exchanger. *Geothermics* **2014**, *51*, 470–482. [CrossRef]
10. Ramesh, K.; Oudina, F.M.; Souayeh, B. *Mathematical Modelling of Fluid Dynamics and Nanofluids*; CRC Press: Boca Raton, FL, USA, 2023.
11. Mebarek-Oudina, F.; Chabani, I. Review on nano-fluids applications and heat transfer enhancement techniques in different enclosures. *J. Nanofluids* **2022**, *11*, 155–168. [CrossRef]
12. Bouselsal, M.; Mebarek-Oudina, F.; Biswas, N.; Ismail, A.A.I. Heat Transfer Enhancement Using Al_2O_3-MWCNT Hybrid-Nanofluid inside a Tube/Shell Heat Exchanger with Different Tube Shapes. *Micromachines* **2023**, *14*, 1072. [CrossRef]
13. Zanchini, E.; Lazzari, S.; Priarone, A. Improving the thermal performance of coaxial borehole heat exchangers. *Energy* **2010**, *35*, 657–666. [CrossRef]
14. Chen, K.; Zheng, J.; Li, J.; Shao, J.; Zhang, Q. Numerical study on the heat performance of enhanced coaxial borehole heat exchanger and double U borehole heat exchanger. *Appl. Therm. Eng.* **2022**, *203*, 117916. [CrossRef]
15. Gascuel, V.; Raymond, J.; Rivard, C.; Marcil, J.S.; Comeau, F.A. Design and optimisation of deep coaxial borehole heat exchangers for cold sedimentary basins. *Geothermics* **2022**, *105*, 102504. [CrossRef]
16. Jia, L.; Cui, P.; Liu, Y.; Lu, L.; Fang, Z. Analytical heat transfer model for coaxial heat exchangers based on varied heat flux with borehole depth. *Appl. Therm. Eng.* **2023**, *218*, 119317. [CrossRef]
17. Abdelhafiz, M.M.; Oppelt, J.F.; Brenner, G.; Hegele, L.A., Jr. Application of a thermal transient subsurface model to a coaxial borehole heat exchanger system. *Geoenergy Sci. Eng.* **2023**, *227*, 211815. [CrossRef]
18. Rajeh, T.; Al-Kbodi, B.H.; Yang, L.; Zhao, J.; Zayed, M.E. A novel oval-shaped coaxial ground heat exchanger for augmenting the performance of ground-coupled heat pumps: Transient heat transfer performance and multi-parameter optimization. *J. Build. Eng.* **2023**, *79*, 107781. [CrossRef]
19. Sun, L.; Fu, B.; Wei, M.; Zhang, S. Analysis of Enhanced Heat Transfer Characteristics of Coaxial Borehole Heat Exchanger. *Processes* **2022**, *10*, 2057. [CrossRef]
20. Pérez-Zárate, D.; Santoyo, E.; Acevedo-Anicasio, A.; Díaz-González, L.; García-López, C. Evaluation of artificial neural networks for the prediction of deep reservoir temperatures using the gas-phase composition of geothermal fluids. *Comput. Geosci.* **2019**, *129*, 49–68. [CrossRef]

21. Tut Haklidir, F.S.; Haklidir, M. Prediction of reservoir temperatures using hydrogeochemical data, Western Anatolia geothermal systems (Turkey): A machine learning approach. *Nat. Resour. Res.* **2020**, *29*, 2333–2346. [CrossRef]
22. El Jery, A.; Khudhair, A.K.; Abbas, S.Q.; Abed, A.M.; Khedher, K.M. Numerical simulation and artificial neural network prediction of hydrodynamic and heat transfer in a geothermal heat exchanger to obtain the optimal diameter of tubes with the lowest entropy using water and Al_2O_3/water nanofluid. *Geothermics* **2023**, *107*, 102605. [CrossRef]
23. Tan, Y.; Guo, L.; Gao, H.; Zhang, L. Deep coupled joint distribution adaptation network: A method for intelligent fault diagnosis between artificial and real damages. *IEEE Trans. Instrum. Meas.* **2020**, *70*, 3507212. [CrossRef]
24. Zhong, K.; Zhou, G.; Deng, W.; Zhou, Y.; Luo, Q. MOMPA: Multi-objective marine predator algorithm. *Comput. Methods Appl. Mech. Eng.* **2021**, *385*, 114029. [CrossRef]
25. Ramezani, M.; Bahmanyar, D.; Razmjooy, N. A new improved model of marine predator algorithm for optimisation problems. *Arab. J. Sci. Eng.* **2021**, *46*, 8803–8826. [CrossRef]
26. Zhao, S.; Wu, Y.; Tan, S.; Wu, J.; Cui, Z.; Wang, Y.G. QQLMPA: A quasi-opposition learning and Q-learning based marine predators algorithm. *Expert Syst. Appl.* **2023**, *213*, 119246. [CrossRef]
27. Sun, L.; Fu, B.; Wei, M.; Zhang, S. New Coaxial Borehole Heat Exchanger Strengthens Heat Transfer Research. *Chin. Hydraul. Pneum.* **2023**, *47*, 164–173.
28. Nakhchi, M.E.; Esfahani, J.A. Numerical investigation of heat transfer enhancement inside heat exchanger tubes fitted with perforated hollow cylinders. *Int. J. Therm. Sci.* **2020**, *147*, 106153. [CrossRef]
29. Caulk, R.A.; Tomac, I. Reuse of abandoned oil and gas wells for geothermal energy production. *Renew. Energy* **2017**, *112*, 388–397. [CrossRef]
30. Xing, L.; Spitler, J.D. Prediction of undisturbed ground temperature using analytical and numerical modeling. Part I: Model development and experimental validation. *Sci. Technol. Built Environ.* **2016**, *23*, 787–808. [CrossRef]
31. Webb, R.L. Perform ance evaluation criteria for use of enhanced heat transfer surfacesin heat exchanger design. *Int. J. Heat Mass Transf.* **1981**, *24*, 715–726. [CrossRef]
32. Mei, R. An approximate expression for the shear lift force on a spherical particle at finite Reynolds number. *Int. J. Multiph. Flow* **1992**, *18*, 145–147. [CrossRef]
33. Gnielinski, V. New equations for heat and mass transfer in turbulent pipe and channel flow. *Int. Chem. Eng.* **1976**, *16*, 359–368.
34. Petukhov, B.S. Heat transfer and friction in turbulent pipe flow with variable physical properties. *Adv. Heat Transf.* **1970**, *6*, 503–564.
35. Garcia, A.; Vicente, P.G.; Viedma, A. Experimental study of heat transfer enhancement with wire coil inserts in laminar-transition-turbulent regimes at different Prandtl numbers. *Int. J. Heat Mass Transf.* **2005**, *48*, 4640–4651. [CrossRef]
36. Liu, Y.; Zhang, Y.; Pei, C.; Wang, Z.; Zhang, W. Evaluation on heat transfer performance of horizontal liquid-solid circulating fluidised bed heat exchanger. *Chem. Ind. Eng. Prog.* **2016**, *35*, 3421–3425.
37. Faramarzi, A.; Heidarinejad, M.; Mirjalili, S.; Gandomi, A.H. Marine Predators Algorithm: A nature-inspired metaheuristic. *Expert Syst. Appl.* **2020**, *152*, 113377. [CrossRef]
38. Hassan, M.H.; Yousri, D.; Kamel, S.; Rahmann, C. A modified marine predators algorithm for solving single-and multi-objective combined economic emission dispatch problems. *Comput. Ind. Eng.* **2021**, *164*, 107906. [CrossRef]
39. Bartumeus, F.; Catalan, J.; Fulco, U.L.; Lyra, M.L.; Viswanathan, G.M. Optimising the encounter rate in biological interactions: Lévy versus Brownian strategies. *Phys. Rev. Lett.* **2002**, *88*, 097901. [CrossRef] [PubMed]
40. Filmalter, J.D.; Dagorn, L.; Cowley, P.D.; Taquet, M. First descriptions of the behavior of silky sharks, Carcharhinus falciformis, around drifting fish aggregating devices in the Indian Ocean. *Bull. Mar. Sci.* **2011**, *87*, 325–337. [CrossRef]
41. Mohammed, H.A.; Abbas, A.K.; Sherif, J.M. Influence of geometrical parameters and forced convective heat transfer in transversely corrugated circular tubes. *Int. Commun. Heat Mass Transf.* **2013**, *44*, 116–126. [CrossRef]
42. Ran, Y.; Bu, X. Influence analysis of insulation on performance of single well geothermal heating system. *CIESC J.* **2019**, *70*, 4191–4198.